

## INVERSION OF MICROSEISMIC ARRAY CROSS SPECTRA

BY RÜDIGER SZELWIS

### ABSTRACT

So-called classical microseisms in a frequency range of about  $f \approx 0.15$  Hz were analyzed by linear least-squares inversion of (cross-) spectra of the components of motion observed in a three-station array on the Island of Sylt (North Sea). As a result of initial data inspection, the analysis was based on a model composed of Rayleigh and Love waves which are incident from one directional sector. The variable model parameters used in the procedure of fitting the model to the data were: (1) directional spread of the incoming "wave beam", (2) "transfer coefficients", standing for modal spectral densities relative to the transfer functions of the local subsurface structure, and (3) shear-wave velocities of the sedimentary sequence extending to 3.7 km depth.

For the two applications presented, the optimal models are statistically consistent representations of the observations. Concerning the sedimentary shear-wave velocities, realistic estimates were obtained for the upper (Cenozoic, Cretaceous, and Triassic) layers, whereas the velocity of the bottom layer was not uniquely resolved.

Concerning transfer coefficients and directional spread, they are well suited for delivering quantitative evidence about the spectrum of the source(s).

### INTRODUCTION

The nature of microseisms in the frequency band  $f \approx 0.05$  to 0.5 Hz has been the object of numerous investigations. An important tool for separation of the wave components involved has been frequency-wave number analysis with seismic arrays of large aperture. Details about the mode structure of the elastic surface-wave components are known, namely from investigations with the Large Aperture Seismic Array (LASA) in Eastern Montana. The three lowest Rayleigh modes ( $f \approx 0.05$  to 0.3 Hz) and the fundamental Love mode ( $f \approx 0.05$  to 0.2 Hz) have been identified. In addition, compressional body waves have been found to dominate above  $f \approx 0.2$  Hz (Toksöz and Lacoss, 1968; Lacoss *et al.*, 1969; Haubrich and McCamy, 1969).

The LASA findings can be regarded as valid for microseisms in general for the frequency range considered, although individual details will have been determined by the geological particularities of the inner-continental location. For example, analysis of the noise structure at the Norwegian Seismic Array (NORSAR) in Southern Norway shows no body-wave components (Bungum *et al.*, 1971).

Going beyond identification of the modes involved in the microseismic motion, Haubrich and McCamy (1969) analyzed the distribution of spectral density among them and found the contribution of individual modes to be strongly frequency dependent.

This frequency structure is determined by the influence of the microseism source as well as by the transfer characteristics of the wave carrying medium. Apparently no attempt has been made up to now to differentiate between these two effects.

In the present paper the mode structure of the microseismic wave field will be determined relative to the transfer characteristics of the local subsurface structure. This is a prerequisite for making quantitative statements about the microseismic sources.

## DATA

In September of 1975 microseisms were recorded in a three-station array on the Island of Sylt, which lies on the southeast margin of the North Sea (Figure 1). Each station consisted of three seismometers (natural frequency,  $f \approx 0.07$  Hz), which were arranged perpendicular to each other for registering the East, North, and vertical components of ground velocity. The recordings were of 20 to 30 min duration.

The time series from the nine seismic channels of the array were assumed to be realizations of a random process, stationary and homogeneous over the restricted time and space intervals considered. Accordingly, estimates of spectral and cross-spectral density have been computed for the frequency interval  $f = 0.05$  to 0.5 Hz. The stability of the estimates corresponds to 27 degrees of freedom; the frequency spacing of  $\Delta f = \frac{1}{128}$  Hz corresponds to  $\frac{3}{4}$  of the resolved bandwidth. All spectra were corrected for the seismometer response, including total system response.

A total of 100 recordings were analyzed with regard to localization of microseismic generation (Schmalfeldt, 1978). Two selected runs will be subjected here to a more detailed analysis, R 28 from September 16, 1975 at 1800 hr and R 45 from September 22, 1975 at 1300 hr.

In both cases, distinct spectral density maxima occur in the frequency range  $f \approx 0.12$  to 0.20 Hz (Figure 2, a and b).

The frequency range is also characterized by a high coherence and stable phases between (corresponding components of) different stations, which is typical for narrow-beam propagating waves. The analysis will concentrate on this frequency range.

## DEFINITION OF THE MODEL

Using the tripartite method, directions of incidence and phase velocities were estimated from the phase spectra of corresponding components. The station pairs (1)-(2) and (2)-(3) as well as (2)-(1) and (1)-(3), were evaluated independently for the ten frequency points of the analysis interval. The direction estimates are given as histograms in Figure 3, a and b. The central value on the abscissa is equal to the median; the class interval width of  $10^\circ$  was chosen according to the assumed mean error of the estimates. Since the estimates show no clear frequency dependence, which is evident from Figure 14, the histograms give a rough measure of the directional distribution of the incoming wave field.

The phase-velocity estimates lie in the range of the dispersion curves for surface waves of a simple layer model of the local subsurface structure.

Consistent with these findings, the analysis will be based on the assumption that microseisms is a stationary and homogeneous field of linear free elastic surface waves. A formal implication is that the (cross-) spectral density may be represented by superposition of mode contributions

$$\begin{aligned} \bar{S}_{ij}^{\nu\mu} &\equiv \bar{C}_{ij}^{\nu\mu} - i\bar{Q}_{ij}^{\nu\mu} \equiv |\bar{S}_{ij}^{\nu\mu}| \exp\{i\bar{\vartheta}_{ij}^{\nu\mu}\} \\ &= \sum_n \int_{-\pi}^{\pi} F^{(n)}(\theta) T_i^{(n)} T_j^{(n)*} \exp\{ik_n r^{\nu\mu} \cos(\theta - \alpha^{\nu\mu})\} d\theta, \end{aligned} \quad (1)$$

where  $C_{ij}$  = cospectrum,  $Q_{ij}$  = quadspectrum,  $\vartheta_{ij}$  = phase;  $i, j$  = indices of the components of motion;  $\nu, \mu$  = indices of sensor locations;  $(r, \alpha)$ , polar coordinates of the vector connecting two sensor locations;  $(k, \theta)$ , polar coordinates of the horizontal

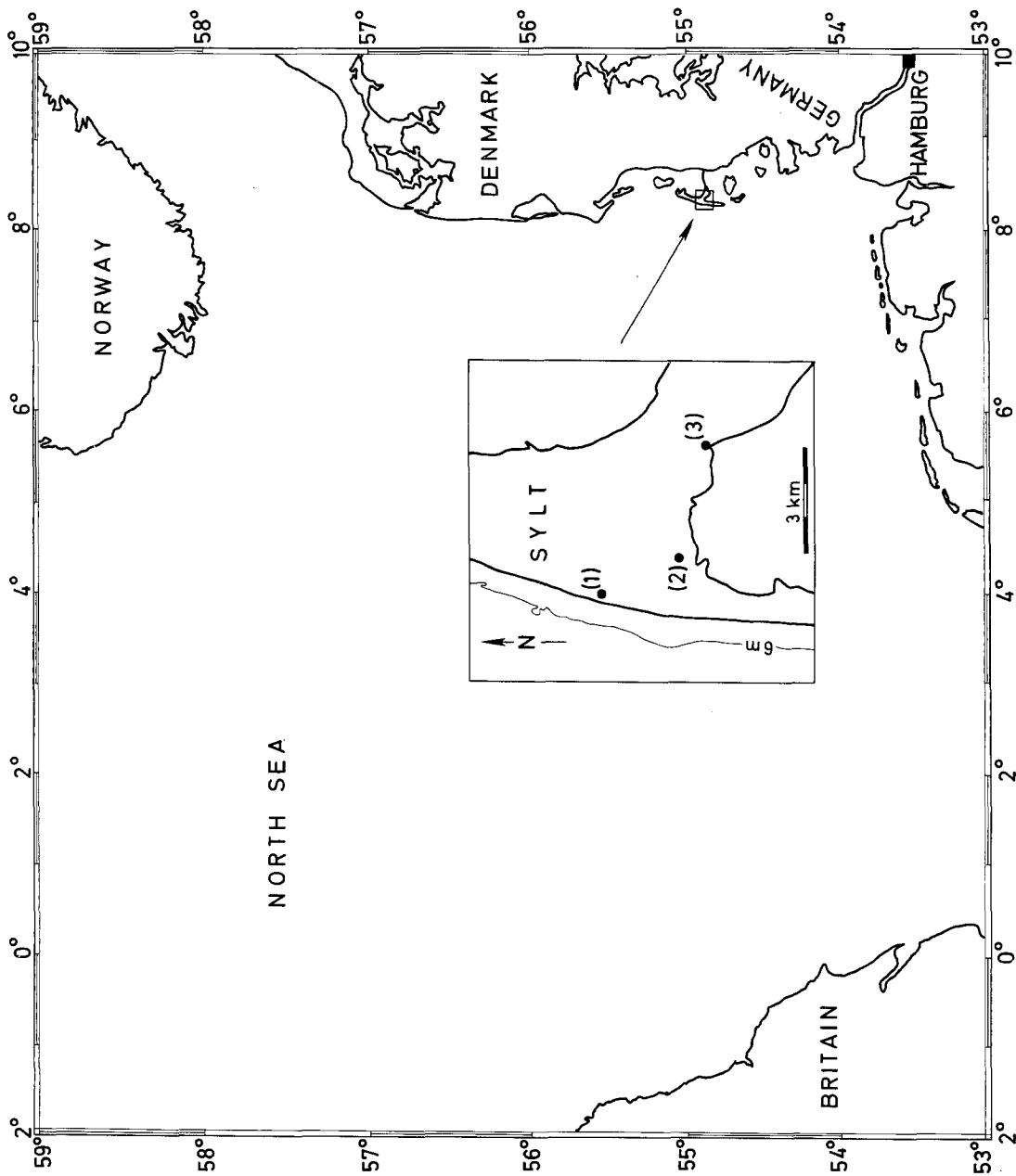


FIG. 1. Location of the 3-station array, each station equipped with three seismometers for the components of ground velocity.

wavenumber vector;  $n =$  mode index;  $F^{(n)}(\theta) =$  directional mode-energy spectrum;  $T^{(n)} =$  transfer function; asterisk denotes complex conjugate. The frequency dependence is not expressed in equation (1).

The relation is based on a right-angle Cartesian coordinate system, the 1-, 2-, and 3-axes of which lie parallel to the geographical E, N, and downward directions, respectively. The polar angle is measured counterclockwise to the 1-(E-) axis.

By equation (1) the "mode (cross-) spectral densities" which add to the theoretical (cross-) spectral density are given as different moments of the "directional mode-energy spectrum". The latter is assumed to be adequately parameterized by

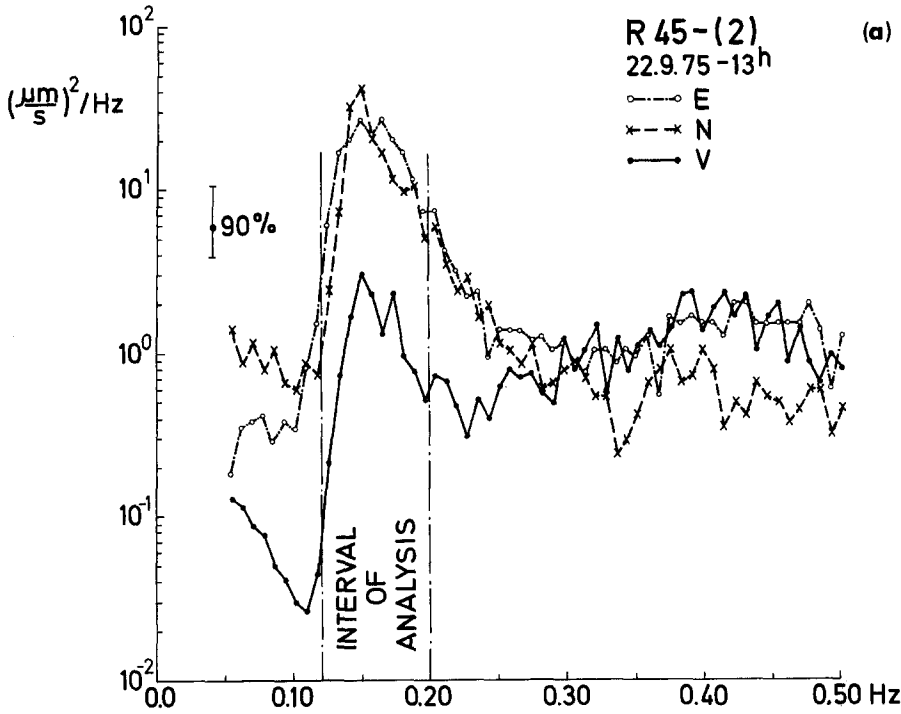


FIG. 2. (a) Run R 45; spectral density of the East, North, and vertical component of motion at station (2). The (cross-) spectral values of the interval of analysis serve as "observations" in the inversion.

$$F^{(n)}(f, \theta) = E^{(n)}(f)\sigma(\theta) \quad \text{where} \quad \sigma(\theta) = \frac{1}{2\sqrt{\pi}} \frac{\Gamma(s+1)}{\Gamma\left(s+\frac{1}{2}\right)} \left| \cos \frac{\theta - \bar{\theta}}{2} \right|^{2s} \quad (2)$$

thus

$$\int_{\bar{\theta}-\pi}^{\bar{\theta}+\pi} F^{(n)}(f, \theta) d\theta = E^{(n)}(f);$$

$f =$  frequency,  $\bar{\theta} =$  mean direction of wave incidence,  $s =$  directional spread parameter,  $\Gamma =$  Gamma Function.

Expression (2) will be discussed in a later chapter. The explicit form for the "directional distribution"  $\sigma(\theta)$  enables additive *a priori* information concerning the type of waves involved. In both of the considered cases, R 45 and R 28, the energy enters from the North and is thus virtually parallel to one of the seismometer components. Coherence and phase between *N* and *V* components are consistent with elliptical polarization in the direction of propagation, while no definite statements can be made about the vertical planes E-N and E-V, respectively.

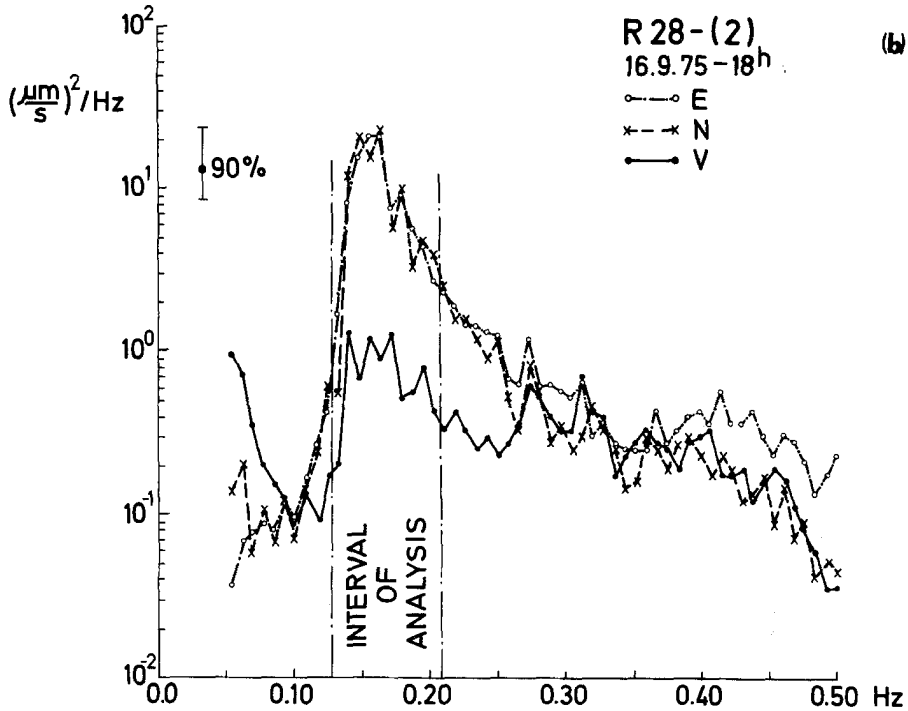


FIG. 2. (b) Run R 28; for legend, see Figure 2a.

The hypothesis that the wave field is essentially composed of narrow-beam Rayleigh waves would imply

- (a) The beam width  $\theta_s$  is obtainable from the spectra of one station according to the relationship

$$\theta_s^2 = 1 - \frac{Q_{13}^2 + Q_{23}^2}{S_3(S_1 + S_2)} \approx \int_{-\pi}^{\pi} \sigma(\theta)(\theta - \bar{\theta})^2 d\theta \tag{3}$$

with  $0 \leq \theta_s \leq 1$ . According to the values determined from the observational spectra the directional focusing is strongest near the spectral density maximum. For case R 45  $\theta_{s,\min}^2 \approx 0.69$  and for case R 28  $\theta_{s,\min}^2 \approx 0.52$ .

Basing the normalized directional distribution  $\sigma(\theta)$ , the second moment of which is the beam width squared, on the model (2), the equivalent parameter values are  $s \approx 2.3$  and  $s \approx 3.3$ . The corresponding directional distributions are presented in Figure 3, a and b. Hence, in both cases  $\theta_{s,\min}$  suggests a greater beam width than would be expected from the histogram of the entire set of estimated incidence directions.

NUMBER OF  
DIRECTION ESTIMATES

(a)

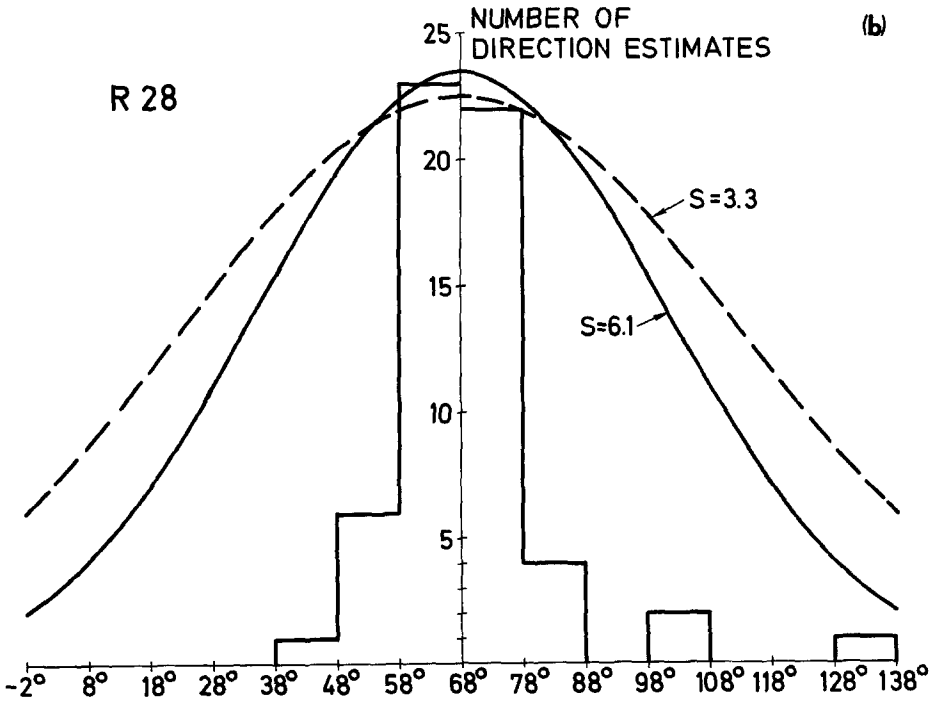
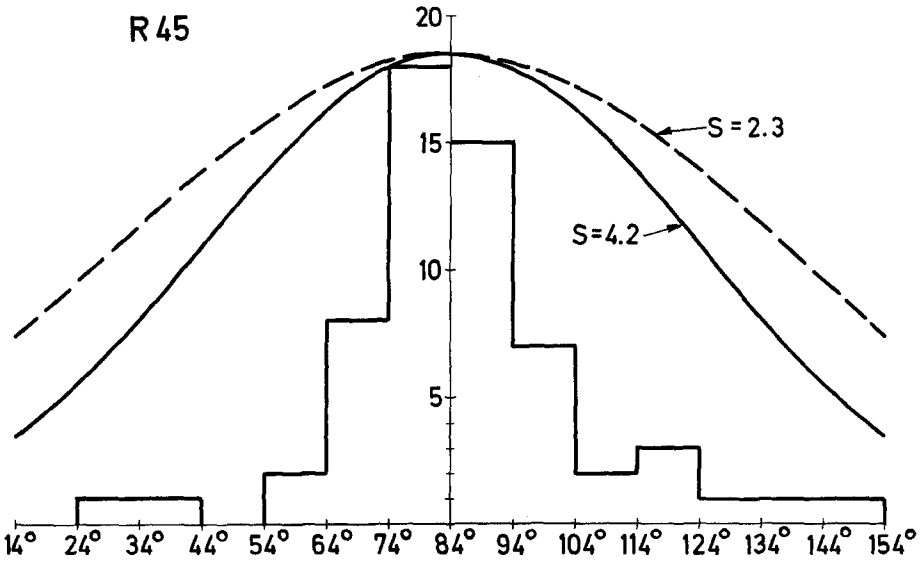


FIG. 3. (a) Run R 45; histogram of the directions of wave incidence, estimated at each frequency point of the interval of analysis by use of the tripartite method. The solid and dashed curves represent models of the directional distribution, computed with  $\sigma(\theta; s)$  [cf. equation (2)] for different values of  $s$ . (b) Run R 28; for legend, see Figure 3a.

- (b) The spectral density ratio of the horizontal components of motion is dependent solely on the directional focusing. Figure 4 compares the values for  $S_1/S_2$  determined from the observational spectra with those calculated on the basis of the model (2) for various values of the parameter  $s$ .

The general similarity between the values from the individual stations shows a distinct frequency dependence in case R 45. Accordingly, the assumed Rayleigh-wave model is only valid in the immediate vicinity of the spectral density maximum. In higher and lower frequency ranges for R 45 and almost the entire frequency range for R 28, the observational values are too large to be consistently explained by narrow-beam Rayleigh waves.

An alternative model which fits the observations better and which is in agreement with findings of numerous authors (for example D'Henry, 1950; Båth, 1952; Gutenberg, 1955; Darbyshire, 1964; Toksöz and Lacoss, 1968; Lacoss *et al.*, 1969; Haubrich and McCamy, 1969), consists of Rayleigh and Love waves incident from the same direction sector. Relating to this model

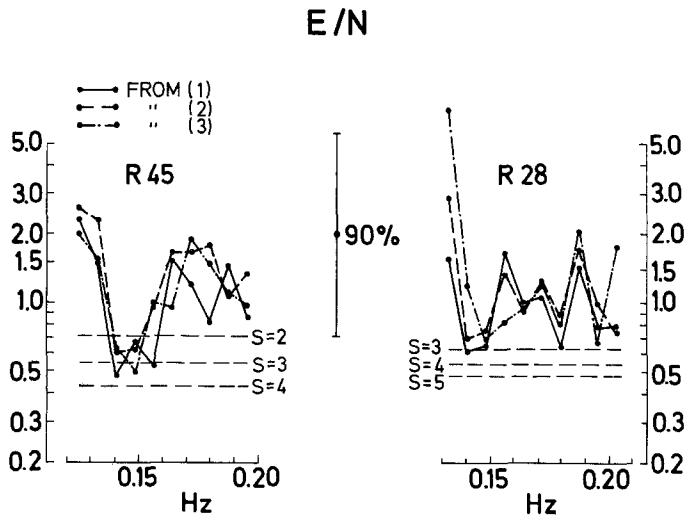


FIG. 4. Ratio of East-to-North component spectral densities. Connected solid circles give observational values, the dashed horizontal lines were computed assuming pure Rayleigh waves of varying beam width.

- (a) The observational  $\theta_s$  values are too high (corresponding to  $s$  values which are too low), because Love waves influence  $S_1$  and  $S_2$ , but not  $S_3$ ,  $Q_{13}$ , and  $Q_{23}$ .
- (b) The ratio  $S_1/S_2$  is largely determined by the spectral density ratio between Love and Rayleigh waves.

### LOCAL CRUSTAL STRUCTURE

This model is taken as basis for the inversion of the array (cross-) spectra in the considered frequency range. The transfer functions in equation (1) then refer to Rayleigh and Love waves of the local subsurface structure. They can be determined by assuming random generating fields acting on the free surface of the layer system (cf. Hasselmann, 1963).

A model of the local subsurface may be established on grounds of geological and geophysical evidence. Geologically speaking, the site of the recordings is part of a

larger unit, the so-called West Schleswig Block, which is characterized by quiet, slightly inclined layering. The compressional ( $P$ -) wave velocities in the sediment are well known from seismic investigations (Hinz, 1964; Heybroek *et al.*, 1967; Essen *et al.*, 1973). They are presented in the third column of Table 1 as parameters of a layer model of horizontal, laterally homogeneous elastic layers. Two superficial layers with  $P$ -wave velocities of 1.7 and 1.86 km/sec, whose thicknesses (about 0.1 km, each) are relatively uncertain, have been included in the uppermost model layer.

The layer densities have been assigned  $P$ -wave velocities according to the Nafe-Drake relation.

The shear ( $S$ -) wave velocities of the near-surface sediments are less well known. Their influence on the dispersion of surface waves in the considered frequency range is sizable, particularly with regard to the ellipticity of Rayleigh waves, i.e., the ratio of horizontal to vertical component of motion (cf., for example, Boore and Toksöz,

TABLE 1  
UPPER CRUST AT THE RECORDING SITE (SYLT)\*

Layer Thickness (km)	Geological Formation	Density (g/cm <sup>3</sup> )	Compressional Wave Velocity (km/sec)	Shear-Wave Velocity (km/sec)	Bias	90%-Confidence Interval (km/sec)	Poisson's Ratio
0.7	Cenozoic	2.0	1.9	0.80	0.08	0.03	0.39
				0.77	0.10	0.03	0.40
1.2	Cretaceous	2.2	3.0	1.49	0.23	0.03	0.34
				1.50	0.28	0.03	0.33
1.0	Triassic	2.5	4.1	2.25	0.56	0.06	0.28
				2.26	0.59	0.04	0.28
0.8	Zechstein rock salt	2.6	4.8	2.78	0.74	0.05	0.25
				2.76	0.74	0.03	0.25
7.8	Palaeozoic	2.8	6.0	$6/\sqrt{3}$	—	—	0.25

\* The layer sequence shown is part of a model consisting of six homogeneous layers over a half-space. The elastic parameters are drawn from other seismic investigations except for the shear-wave velocities of the upper four sedimentary layers, which have been estimated with the inversion procedure. The estimates and corresponding statistics result from runs R 45 (upper value) and R 28 (lower value), respectively.

1969; Asten, 1978). As a consequence, they will act as variable parameters in the inversion procedure.

The pre-Zechstein geology of the recording site is extrapolated from seismic results for the adjacent mainland (Hirschleber, 1975). Thus, the layer model is completed by a layer for the crystalline upper crust (thickness, 7 km;  $P$ -wave velocity, 6.0 km/sec) and the lower crust (20 km; 6.6 km/sec), overlying a homogeneous mantle substratum (infinite depth, 8.1 km/sec). The corresponding  $S$ -wave velocities are derived from the Poisson relationship, according to which the  $P$ - and  $S$ -wave velocities differ by a factor of  $\sqrt{3}$ . Again, the densities follow the Nafe-Drake relationship.

#### DIRECTIONAL MODE-ENERGY SPECTRUM

The wave mode model implies an energy distribution which is concentrated on circles in the wavenumber plane with radius  $k_n(f)$ ,  $n$ -mode index. Based on evidence

from the rough estimates, the directional mode-energy spectrum is separated into a direction-dependent factor (“directional distribution”) and a modal frequency-dependent factor (“transfer coefficients”). The directional distribution is modeled by a symmetrical function  $\sigma(\theta)$ , [equation (2)], the mean of which is defined to be the central value of the histogram of direction estimates (Figure 3, a and b). While this is considered to be sufficiently accurate, the spread parameter  $s$  figures as an unknown. The significance of the transfer coefficients  $E^{(n)}(f)$  becomes obvious by looking at the spectral density and its partition among contributing modes

$$\tilde{S}_{ii}^{rr} \equiv \tilde{S}_i = \sum_n \tilde{S}_i^{(n)} \tag{4}$$

[cf. equation (1)].

The modal contributions to the spectral density of the vertical component and of the sum of horizontal components follow the directionally-independent relations

$$\begin{aligned} \tilde{S}_3^{(n)} &= R^{(n)}V^{(n)} \\ \tilde{S}_1^{(n)} + \tilde{S}_2^{(n)} &= R^{(n)}H^{(n)} + L^{(n)}T^{(n)} \end{aligned} \tag{5}$$

where

$$V^{(n)} \equiv |{}^R T_3^{(n)}|^2, \quad H^{(n)} \equiv |{}^R T_1^{(n)}|^2 + |{}^R T_2^{(n)}|^2, \quad T^{(n)} \equiv |{}^L T_1^{(n)}|^2 + |{}^L T_2^{(n)}|^2.$$

(The indices  $R$  and  $L$  refer to Rayleigh and Love waves, respectively, and  $R^{(n)}$  and  $L^{(n)}$  stand for  $E^{(n)}$  for Rayleigh and Love waves). It follows from equation (5), that  $E^{(n)}$  represents the mode spectral density relative to the transfer functions. The structure of the transfer functions determines the number of modes which essentially contribute to energy transport. Anticipating a result, in both cases, R 45 and R 28, no more than the three lowest Rayleigh modes and the fundamental Love mode prove to be relevant. In fact, in the considered frequency interval the quotients of the transfer functions

$$T^{(m)}/T^{(o)}, \quad V^{(n)}/V^{(o)}, \quad H^{(n)}/H^{(o)}, \quad m = 1, 2, \dots; n = 3, 4, \dots;$$

are smaller than 0.01. The analog is then valid for the ratio of the corresponding spectral densities generated by a white spectrum source.

If this is regarded as *a priori* information, then the unknown transfer coefficients are:  $R^{(n)}(f_j)$ ,  $L^{(o)}(f_j)$ ;  $n = 0, 1, 2$ ;  $j = 1, \dots, N$  ( $N =$  number of frequency points).

### PROCEDURE

The theoretical (cross-) spectral density (1) is thus defined as a function of the  $4N + 5$  unknown parameters  $E^{(n)}(f)$ ,  $s$ , and the sedimentary shear-wave velocities in the layer system. The following spectra have been computed

- (a) the spectral densities ( $\tilde{S}_i$ ,  $i = 1, 2, 3$ ) for the three components of motion,
- (b) the cross-spectral densities of non-zero expectancy ( $\tilde{C}_{12}$ ,  $\tilde{Q}_{13}$ ,  $\tilde{Q}_{23}$ ) for different components of one station,
- (c) the cross-spectral densities ( $\tilde{C}_{ii}^{\nu\mu}$ ,  $\tilde{Q}_{ii}^{\nu\mu}$ ,  $i = 1, 2, 3$ ;  $\nu\mu = 12, 13, 23$ ) for corresponding components of the different station pairs.

These  $24N$  real model spectra correspond to  $36N$  real observational spectra.

The variable model parameters are estimated by fitting the model spectra to the observational spectra. This requires that "initial estimates" be known.

Concerning the shear-wave velocities ( $b_i$ ,  $i = 1, 2, 3, 4$ ) of the upper four sediment layers, the following values are considered representative for the geological formations in question:  $b_1 \approx 0.8 - 1.0$  km/sec,  $b_2 \approx 1.5 - 1.6$  km/sec,  $b_3 \approx 2.2 - 2.3$  km/sec,  $b_4 \approx 2.6 - 2.7$  km/sec (Faust, 1951; Nafe and Drake, 1957; Press, 1966).

Hereby rough estimates of the transfer coefficients can be computed from

$$S_3^{(\nu)} \approx \sum_{n=0}^2 R^{(n)} V^{(n)}$$

$$S_1^{(\nu)} + S_2^{(\nu)} \approx \sum_{n=0}^2 R^{(n)} H^{(n)} + L^{(o)} T^{(o)} \quad (6)$$

where  $S_i^{(\nu)}$  is the observational spectral density of the  $i$ -component from station ( $\nu$ ). This is a system of six equations at each frequency point.

An approximate value for the directional spread parameter  $s$  can be derived from the histogram of the direction estimates (Figure 3, a and b).

The formalism of the linear least-squares inversion leading to improved parameter estimates is described in the Appendix.

## RESULTS

Starting from the corresponding initial estimates for the sedimentary shear-wave velocities in both runs, R 45 and R 28, the residual estimates  $\hat{\epsilon}$  inferred from the fitting procedure are plotted in Figure 5. In case R 45 their distribution does not contradict the hypothesis of  $\epsilon$  being a normal random variable. In case R 28 there is a slight departure from unimodality. This will be borne in mind when the normality assumption is needed.

The optimal solution of the weighted system of equations (A2) is determined using a maximum allowed variance of  $t_j \approx 1$  [cf. equation (A4)] for all parameter corrections. It leads to

Run	$p$	$ \hat{\epsilon}_{(p)} ^2$	$\hat{\sigma}_{(p)}^2$	$\varphi_{(p)}^2$	$\gamma_{(p)}^2$
R 45	31	350	1.06	110	0.91
R 28	29	597	1.80	48	0.81

(for definitions see Appendix).

The quantity  $\varphi_{(p)}^2$  exceeds  $F_{30,330}(0.1) \approx 1.5$  [cf. equation (A7)] for both runs; hence, the model is a statistically consistent representation of the data set. According to  $\gamma_{(p)}^2$ , the model accounts for 91 per cent (R 45) and 81 per cent (R 28), respectively, of the data [cf. equation (A8)].

The following results correspond to the number  $p$  of degrees of freedom

(a) Directional spread parameter

Run	$s$	$\delta s$
R 45	4.2	0.8
R 28	6.1	1.5

In both cases the bias defined by (A5) is less than 0.001, so that  $\delta s$  represents half the width of a 90 per cent confidence interval [cf. equation (A6)].

The directional distribution corresponding to the  $s$ -values is given in Figure 3, a and b. For example, 30 per cent of the total energy is concentrated in a direction sector of  $30^\circ$  or  $25^\circ$  width (for cases R 45 and R 28, respectively), symmetrical to the mean direction of incidence.

- (b) Sedimentary shear-wave velocities. The results are given in column four of Table 1. For the interpretation it is important to note that they are only estimates of the corresponding parameters in case of negligible bias. Otherwise one is dealing with estimates of linear functions of the parameters and their initial estimates with linear coefficients, which are elements of the resolution matrix  $R^{(p)}$  (cf. Appendix). In case R 45, as well as in case R 28, the resolution matrix shows that the estimates concerning the shear wave velocities are

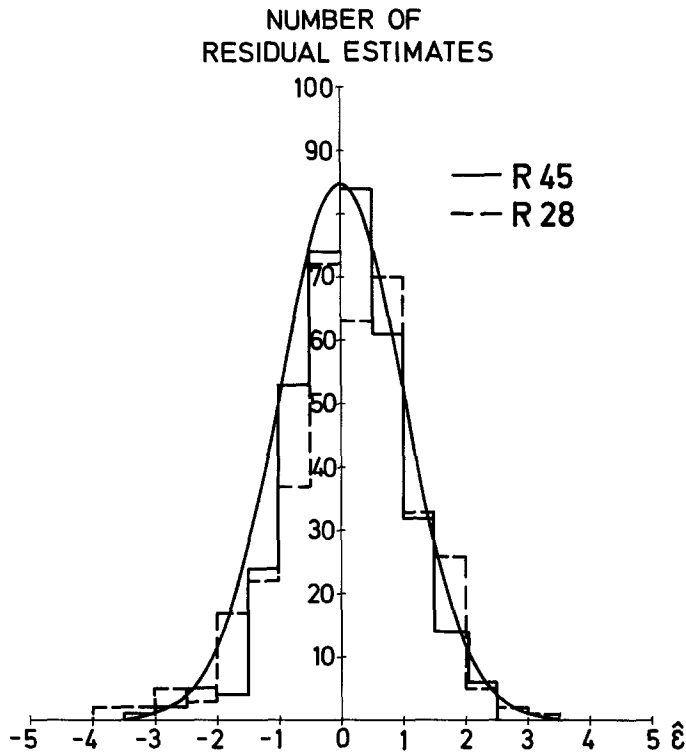


FIG. 5. Histograms of estimated residuals in the fitting procedure. The smooth curve represents a Gaussian distribution with unit variance [cf. introduction of "problem variance" following (A-1)].

dependent on each other, but largely independent of all other model parameters.

Their interdependence is determined for case R 45 by

$$E \begin{pmatrix} \hat{b}_1 \\ \hat{b}_2 \\ \hat{b}_3 \\ \hat{b}_4 \end{pmatrix} = \begin{pmatrix} b_1 \\ b_2 \\ b_3 \\ b_4 \end{pmatrix} + \begin{pmatrix} -0.08 & 0.13 & -0.14 & -0.09 \\ 0.13 & -0.23 & 0.30 & 0.04 \\ -0.14 & 0.30 & -0.56 & 0.30 \\ -0.09 & 0.04 & 0.30 & -0.74 \end{pmatrix} \begin{pmatrix} b_1 - \hat{b}_1 \\ b_2 - \hat{b}_2 \\ b_3 - \hat{b}_3 \\ b_4 - \hat{b}_4 \end{pmatrix}$$

$E$ , expectation;  $\hat{b}_i$ , optimal estimate;  $b_i$ , value to be estimated;  $\hat{b}_i$ , initial estimate.

The symmetric matrix displays the essential constituents of the sum of squares bias measure (A5), the values of which are given in column five of Table 1. Hence, the velocity estimates for the upper two layers are formally acceptable, while the others exhibit non-negligible bias. As to the Triassic layer, the estimate conforms to the representative velocity values cited and therefore still may be acceptable in the sense of a realistic estimate. Regarding the lowest sedimentary layer, the velocity estimate and the corresponding confidence interval are misleading.

It is important to note that the remaining elastic constants of the layer model (Table 1) enter into (1) as error-free parameters. This has to be considered in the interpretation of the confidence interval for a true parameter.

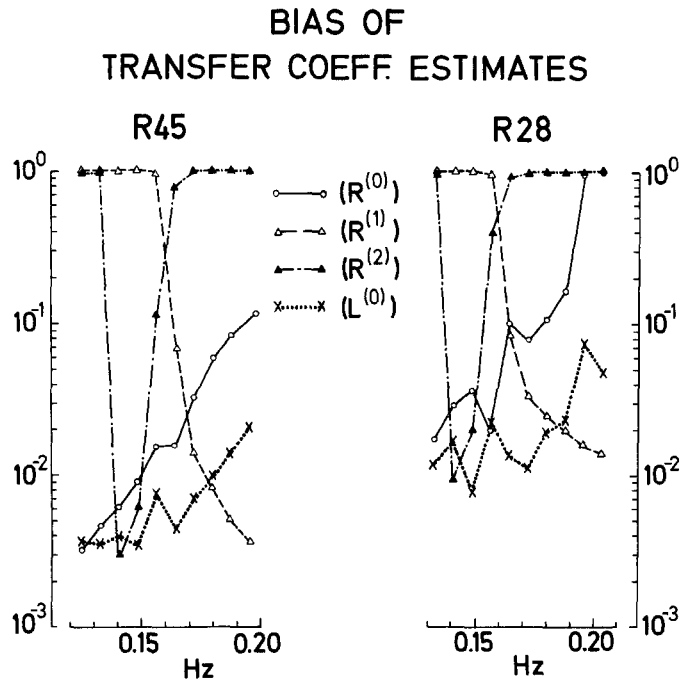


FIG. 6. BIAS, as defined by (A5), associated with the transfer coefficient estimates. Symbols  $R^{(n)}$ ,  $n = 0, 1, 2$  relate to the Rayleigh modes and  $L^{(0)}$  to the fundamental Love mode.

- (c) Transfer coefficients. The estimates concerning the transfer coefficients are affected by a frequency-dependent bias (Figure 6). There is a strong dependence between bias and transfer functions. Large bias values occur when the respective modal transfer function is relatively small and vice versa. This is reflected in the conspicuous frequency trends of the bias curves.

Transfer coefficient estimates are given in Figure 7. Their basic importance lies in the fact that they permit conclusions about the Rayleigh- and Love-wave sources. If one could assume wavenumber-independent source spectra and a laterally homogeneous, conservative medium of wave propagation, the transfer coefficients would then be almost proportional to the source spectra.

Comparing the spectra of  $R^{(0)}$  and  $L^{(0)}$ : In case R 28, the two exhibit analogous peak shapes with apparently coincident peak frequencies; in case R 45,  $L^{(0)}$  seems to be peaked at a frequency  $\Delta f \approx 0.015$  Hz lower than  $R^{(0)}$ .

It is possible that the discrepancy in case R 45 must be attributed to masking of the  $L^{(0)}$  peak by additional (local or distant) disturbances or to a slight spatial displacement of Rayleigh- and Love-wave sources not accounted for by the model. On the other hand, the confidence half-width for  $L^{(0)}$  ( $f < f_{\text{peak}}$ ) tends to exceed  $L^{(0)}$ . Thus, one cannot say with the same certainty as in case  $R^{(0)}$  whether or not one is dealing with a spectral peak.

The peak frequencies of  $R^{(0)}$  are near  $f = 0.15$  Hz in both cases, R 45 and R 28. According to the weather charts, the interaction of oppositely traveling ocean waves due to reflection from the Norwegian Coast would come into question as a source. The Norwegian Coast was recognized long ago as a

TRANSFER COEFFICIENT ESTIMATES

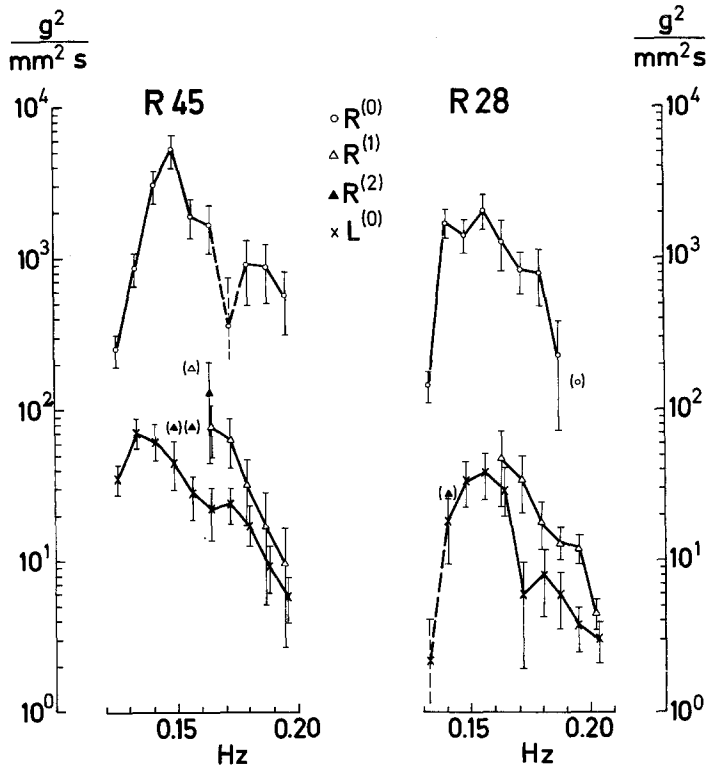


FIG. 7. Transfer coefficients, as defined in equation (2). Estimates associated with  $\text{BIAS} \approx 0.1$  are given together with 90 per cent confidence intervals; the connecting lines are dashed in case the estimate is less than half its confidence interval. Values in braces are associated with  $0.1 \approx \text{BIAS} \approx 0.95$  (cf. Figure 6).

decisive factor for generation of microseisms registered in Northern and Central Europe. This aspect will not be discussed further in this paper.

COMPARISON OF THE MODEL WITH OBSERVATIONS

The given set of parameter estimates constitute the optimal model in the sense of the linear inverse problem. The corresponding theoretical spectra will be compared to the observational spectra in the following figures.

Figures 8 and 9 show the theoretical spectral density of the three components of motion and its partition among contributing modes. It is interesting that the reciprocal dominance of the fundamental and first higher Rayleigh modes in the

vertical component is similar to that found in LASA (cf. Haubrich and McCamy, 1969, Figure 11).

Theoretical and observational componential spectral densities are given together in Figure 10. Here, and in the following figures, the given confidence range represents the error interval incurred in estimating the observational spectra from finite time series, i.e., the interval about the observational spectra, in which the true spectra are to be found on the assumed confidence level. The errors induced for the optimal model have been described with respect to the individual parameters and are not repeated by means of frequency-dependent error bounds for the theoretical spectra.

### THEORETICAL SPECTRAL DENSITY (R45)

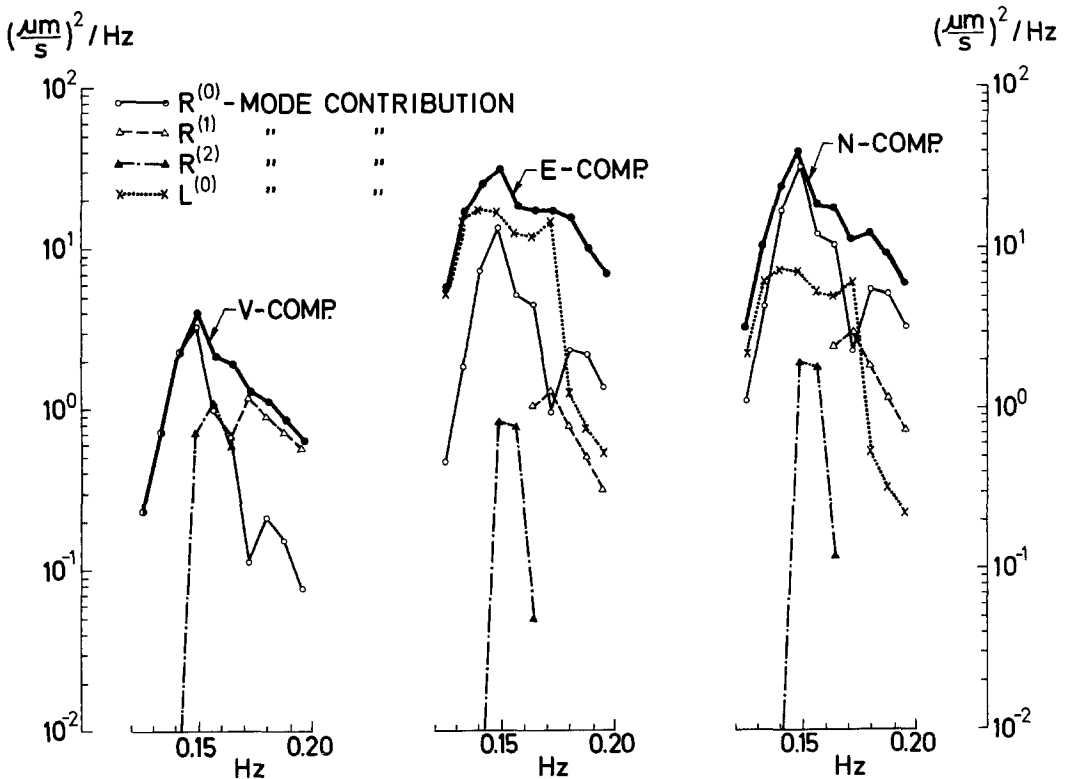


FIG. 8. Run R 45; theoretical spectral density of the three components of motion and its partition among contributing modes. The results given are computed on the basis of transfer coefficient estimates with BIAS < 0.1 only.

Regarding the spectral units, Figure 10 demonstrates the goodness-of-fit in terms of the componential energy density.

Theoretical and observational coherence are shown in Figure 11 for different components of one station and in Figure 12 for corresponding components of the station pair (1)-(2). The plots are on an arctanh scale, where the confidence interval can be represented by a constant interval. In Figure 12 the theoretical coherence systematically exceeds the observational coherence. This may reflect not only the above-mentioned inadequacy of the one-source model, but also inadequate array geometry, since the axis of the near-linear array configuration considerably deviates from the dominant direction of wave approach.

Phase, defined implicitly in (1), is given for corresponding components of station pair (1)-(2) in Figure 13. In addition to observational and theoretical phase, phase curves are given corresponding to unidirectional propagation [ $\sigma(\theta) \rightarrow \delta(\theta - \bar{\theta})$ ], where  $\delta$  is the Dirac function,  $\bar{\theta}$  is the mean direction of incidence of individual modes. They are presented in those frequency ranges in which they contribute significantly to energy transport (cf. Figures 8 and 9).

Concerning the vertical components, theoretical and observational phase are in very good conformity, and the frequency-dependent dominance of the individual Rayleigh modes is well represented.

The horizontal components should reflect the Love-wave contribution, which is

THEORETICAL SPECTRAL DENSITY (R 28)

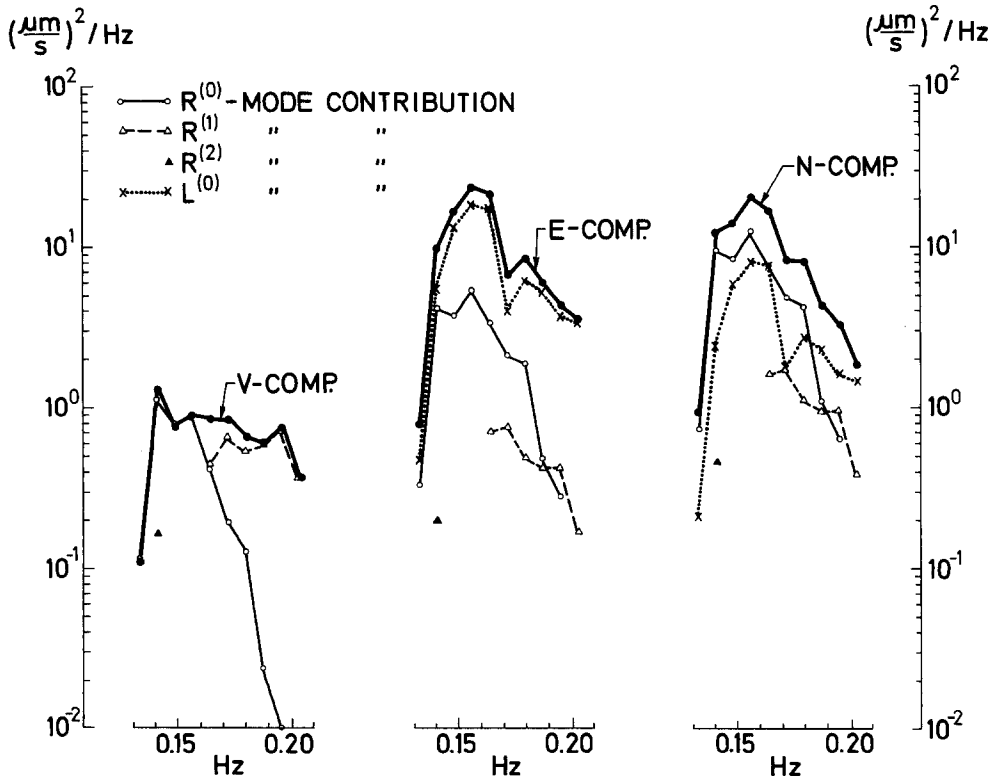


FIG. 9. Run R 28; for legend, see Figure 8.

essentially dominant in the E-components. Considering R 28, the observational (as well as the theoretical) phase indeed follows the phase curve for the fundamental Love mode; however, considering R 45, the evidence for Love waves is poor. In terms of the model, this is due to the ratio of the spectral densities associated with the fundamental Love mode and the Rayleigh modes.

A distortion of the results due to inadequate array geometry is probably not negligible; still, the figure suggests the difficulty of mode separation by use of phase observations alone.

The phase for different components of one station is affected by a relatively large range of uncertainty because of the small degree of coherence (Figure 11). In place of it, the mean direction of Rayleigh-wave incidence is considered, which is calcu-

lated from the phase relations between the vertical and each horizontal component [cf. (A9)].

From Figure 14, the estimates of mean direction of wave incidence obtained by using (A9), on the one hand, and the tripartite method, on the other, vary in relation to one another. On the left-hand side of the frequency axis the estimates roughly coincide; on the right-hand side, they differ by roughly  $180^\circ$ . The reason for this is that on the left side the Rayleigh wave polarization is retrograde, but on the right side it is prograde.

The transition between retrograde and prograde motion, theoretically confined to a frequency point, is unstable in that small variations in the modal contributions to

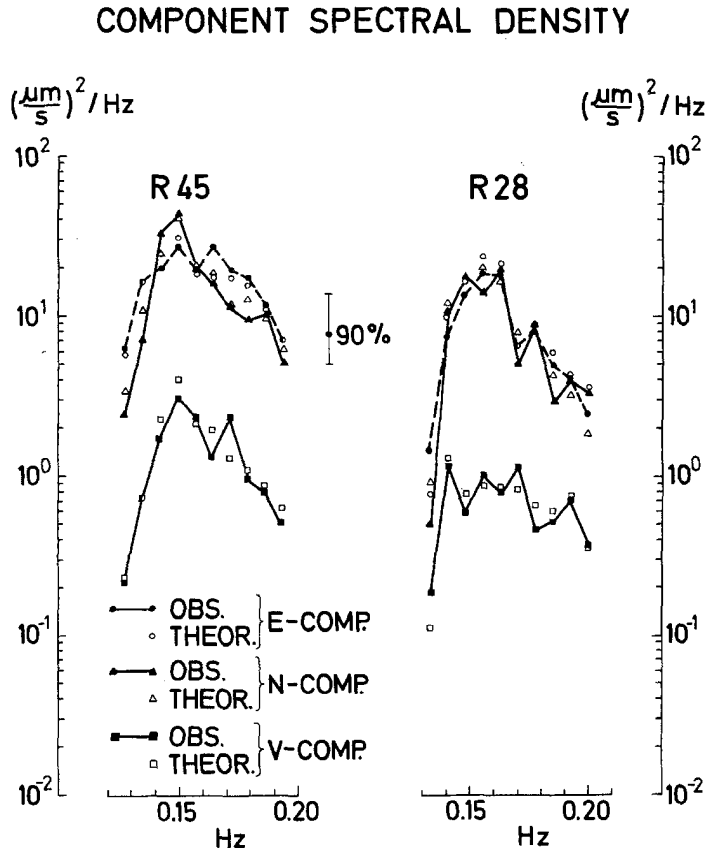


FIG. 10. Comparative spectral densities of the components of motion: (i) observational spectra from station (2) (cf. Figure 2, a and b), and (ii) theoretical model spectra (cf. Figures 8 and 9).

the wave energy around this frequency point can influence the sense of polarization. This is most likely the cause of the major discrepancies between theoretical and observational values, which are present especially in case R 45. Fundamentally, the figure suggests the validity of the theoretical Rayleigh-wave mode structure, as do all comparisons between observational and theoretical quantities which only concern the vertical component of motion and are thus independent of Love-wave influences.

There is no analog for testing the interpretation concerning the Love waves separately, i.e., independent of any Rayleigh-wave model. Indirect support is provided by the consistency of the (total) optimal model with the findings that led to the definition of the model.

CONCLUDING REMARKS

So-called classical microseisms in a frequency range of about  $f \approx 0.15$  Hz were analyzed by inversion of "observational" array cross-spectra on the basis of a model composed of Rayleigh and Love waves which are incident from one directional sector. The variable model parameters used in the procedure of fitting the model to the observations were: (1) directional spread of the incoming "wave beam", (2) "transfer coefficients", standing for mode spectral densities relative to the transfer functions of the local subsurface structure, and (3) shear-wave velocities of the sedimentary sequence extending to 3.7 km depth.

For the two applications presented, the optimal models are statistically consistent

COHERENCE

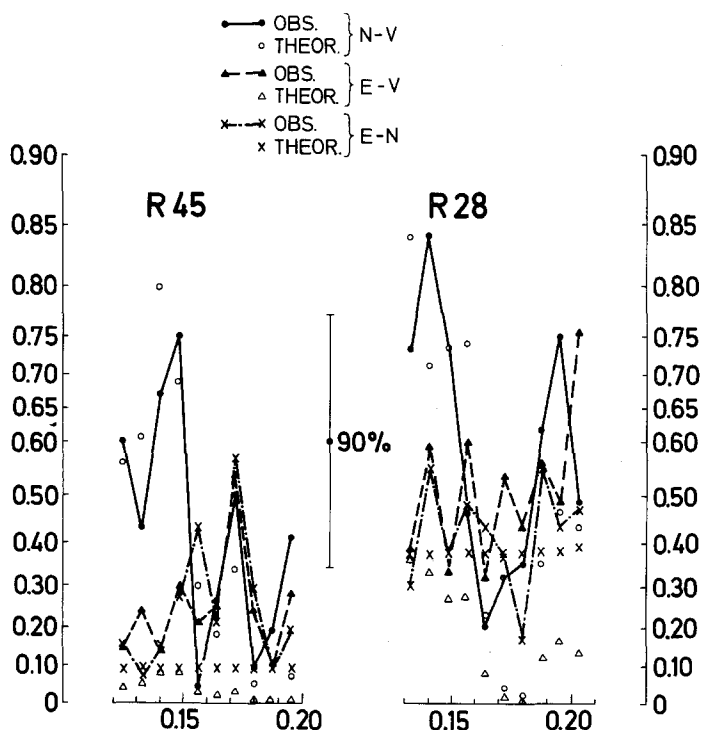


FIG. 11. Comparative coherence for different components of motion at one position: (i) observational coherence from station (2), and (ii) theoretical coherence.

representations of the observations. Concerning the sedimentary shear-wave velocities, realistic estimates were obtained for the upper (Cenozoic, Cretaceous, and Triassic) layers, whereas the velocity of the bottom layer was not uniquely resolved.

Concerning transfer coefficients and directional spread, they are well suited for delivering quantitative evidence about the spectrum of the source(s). This aspect will be considered in a subsequent paper.

APPENDIX

*I. Model fitting.* The inverse problem of determining the unknown (variable) parameters of the model (cross-) spectral density is solved by fitting the model

spectra to the observational spectra. The linear least-squares procedure follows the lines of the generalized matrix inverse technique (cf. Wiggins, 1972).

The first step consists of linearization of the model about the initial parameter estimates. This reduces the problem to solution of a system of linear equations

$$\bar{x}_i = \sum_{j=1}^m \bar{D}_{ij} \bar{y}_j; \quad i = 1, \dots, n; \quad n > m \quad (A1)$$

where  $\bar{x}_i = g_i - \bar{g}_i$ ;  $\bar{y}_j = a_j - \bar{a}_j$ ;  $\bar{D}_{ij} = (\partial \bar{g}_i / \partial a_j)_{\bar{a}}$  and  $g_i, \bar{g}_i, a_j, \bar{a}_j$  represent the vectors of observational spectra, model spectra, variable parameters to be estimated, and

### COHERENCE PAIR OF STATIONS (1) - (2)

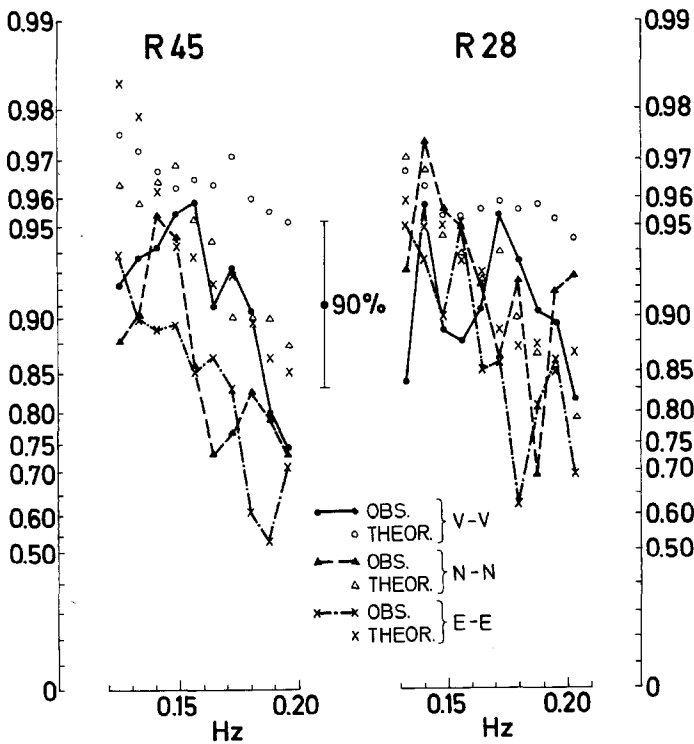


FIG. 12. Observational and theoretical coherence for corresponding components of motion of station pair (1)-(2).

initial parameter estimates, respectively. The system is weighted using

(a) The variance matrix of the observations

$$\bar{X}_{ij} = \text{diag}[\text{var}(g_i)]; \quad i, j = 1, \dots, n.$$

The variances are estimated from the observational spectra using standard methods (cf. Jenkins and Watts, 1968).

(b) The variance matrix of the parameters

$$A_{ij} = \text{diag}[\text{var}^{a.p.}(a_i)]; \quad i, j = 1, \dots, m.$$

Its elements are *a priori* variances of the parameters. With  $G_{ij} = \bar{X}_{ij}/\sigma^2$ ;  $\sigma^2 =$  problem variance, the transformation is written in matrix notation as follows

$$D = G^{-1/2} \bar{D} A^{1/2}, \quad y = A^{-1/2} \bar{y}, \quad x = G^{-1/2} \bar{x},$$

hence, (A1) is replaced by

**PHASE  
PAIR OF STATIONS (1) - (2)**

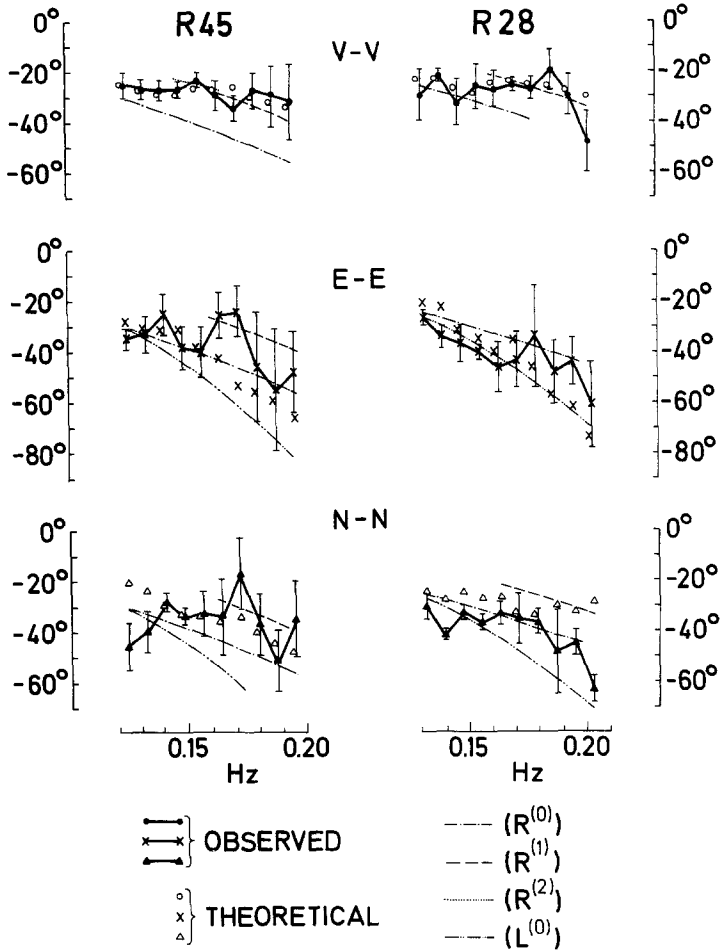


FIG. 13. Observational and theoretical phase for corresponding components of motion of station pair (1)-(2). The fine lines refer to plane waves associated with individual contributing modes.

$$x = Dy. \tag{A2}$$

Solution of the weighted system (A2) by use of the generalized (Moore-Penrose) matrix inverse of  $D$  is equivalent to simultaneously minimizing  $|\epsilon|^2 = |x - Dy|^2$  and  $|y|^2$ . It is based on singular value decomposition

$$D = U \Lambda V',$$

where  $U_{nm}$  resp.  $V_{mm}$  contain the eigenvectors associated with the columns resp. rows of  $D$ ;  $\Lambda_{mm} = \text{diag}(\lambda_j)$  and  $\lambda_j =$  (non-negative) eigenvalues of  $D$ , ranked in decreasing order of magnitude;  $V'$  denotes transpose of  $V$ . Equation (A2) is then solved by

$$\hat{y} = V \Lambda^{-1} U' x \tag{A3}$$

(on the understanding that  $1/\lambda_j = 0$  for  $\lambda_j = 0$ ).

II. *Statistical inference.* The number  $p \leq m$  of degrees of freedom in the data ( $x$ ) is determined by imposing an upper limit on the variance of  $\hat{y}_j$  through

$$\text{var}^{(p)}(\hat{y}_j) = \hat{\sigma}_{(p)}^2 \sum_{k=1}^p \left( \frac{V_{jk}}{\lambda_k} \right)^2 < t_j \tag{A4}$$

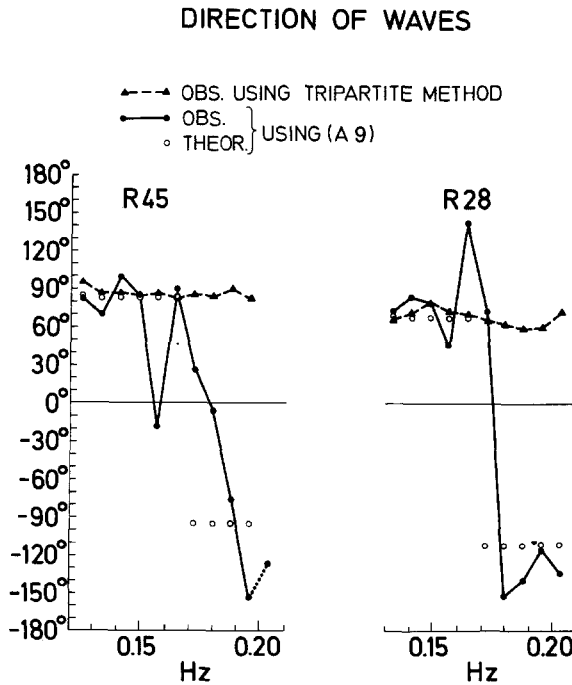


FIG. 14. Comparative wave directions.

(cf. Jackson, 1972). The unbiased problem variance estimate is given by

$$\hat{\sigma}_{(p)}^2 = \frac{|\hat{\epsilon}_{(p)}|^2}{n - p} = \frac{|x - \hat{x}^{(p)}|^2}{n - p}; \quad \hat{x}^{(p)} = U^{(p)} U^{(p)'} x;$$

$U^{(p)}$  is derived from  $U$  by cancellation of the last  $n - p$  columns. Thus, the smallest  $n - p$  singular values  $\lambda_{p+1}, \dots, \lambda_m$  and the corresponding eigenvectors in  $V$  and  $U$  are neglected in the construction of the inverse. The reduction in variance is parallel to an increase in the bias of the parameter correction estimates, equivalent to a reduction in their resolution. Because

$$E(\hat{y}^{(p)}) = V^{(p)} V^{(p)'} y \equiv R^{(p)} y$$

( $E$ , expectation), the solution is only unique for  $p = m$ , when the resolution matrix  $R^{(p)}$  equals the identity matrix. A measure for the bias in the case  $p \leq m$  is

$$\text{BIAS}(\hat{y}_j^{(p)}) = \sum_{k=1}^m (R_{jk}^{(p)} - I_{jk})^2, \quad j = 1, \dots, m \quad (\text{A5})$$

$I$  = identity matrix. If  $\text{BIAS}(\hat{y}_j^{(p)}) \ll 1$ , and the components of the vector of residuals  $\epsilon = x - Dy$ , with  $E(\epsilon) = 0$ ,  $E(\epsilon\epsilon') = \sigma^2 I$ , are normally distributed, a confidence interval may be defined for  $y$ . Hence, a  $100(1 - \alpha)$  per cent confidence interval for  $a_j = \hat{a}_j + y_j$  is given by

$$\hat{a}_j + \hat{y}_j^{(p)} \pm \delta a_j; \quad \delta a_j = z_{\alpha/2} [\text{var}^{(p)}(\hat{y}_j)]^{1/2} \quad (\text{A6})$$

where  $z_{\alpha/2}$  is the  $100\alpha$  percentage point of the standardized normal distribution.

In addition to parameter variance, the quality of the total model may be specified

(a) The expression

$$\varphi_{(p)}^2 = \frac{|x|^2 - |\hat{\epsilon}_{(p)}|^2}{p \hat{\sigma}_{(p)}^2}$$

follows a noncentral  $F$ -distribution with vanishing noncentrality parameter under the null-hypothesis  $Dy = 0$  (cf. Searle, 1971). Hence, with the central  $F_{p,n-p}(\alpha)$  distribution, the inequality

$$\varphi_{(p)}^2 \geq F_{p,n-p}(\alpha) \quad (\text{A7})$$

defines a region where the null-hypothesis is to be rejected, equivalently where the "data are in concordance with the model", on the  $\alpha$ -level of significance.

(b) A different criterium is provided by the correlation coefficient between data vector  $x$  and "model vector"  $\hat{x}^{(p)}$

$$\gamma_{(p)}^2 = \frac{(x' \hat{x}^{(p)})^2}{x' x (\hat{x}^{(p)'} \hat{x}^{(p)})} = \frac{|x|^2 - |\hat{\epsilon}_{(p)}|^2}{|x|^2} \quad (\text{A8})$$

(cf. Searle, 1971). This coefficient of determination represents the fraction of the total sum of squares  $|x|^2$  accounted for by fitting the model.

III. *Consistency test.* The direction of incidence of narrow-beam Rayleigh waves can be estimated by means of a 3-component station according to

$$\bar{\theta}_R \approx \text{Arctan}(Q_{23}/Q_{13}). \quad (\text{A9})$$

The result is only unique if the Rayleigh wave polarization is known. In the underlying coordinate system, (A9) is valid for elliptically retrograde polarization. In the case of prograde polarization  $\bar{\theta}_R$  does not give the direction of incidence, but rather the direction of propagation.

Polarization in the fundamental Rayleigh mode is usually retrograde; the higher modes can be prograde and/or retrograde. Thus in a wave field involving a number of modes, polarization depends on the proportion of energy in the individual modes.

## ACKNOWLEDGMENTS

The author wishes to thank Dipl. Geophys. R. Rudloff and Dr. B. Schmalfeldt for the technical concept and performance of the experiment. He is greatly indebted to Miss D. Ruhle-von-Berg for extensive computer work. The computations were performed on a CD-Cyber 172 and a CD-Cyber 76. The research was supported by the Sonderforschungsbereich 94, Meeresforschung Hamburg, sponsored by the Deutsche Forschungsgemeinschaft.

## REFERENCES

- Asten, M. W. (1978). Geological control on the three-component spectra of Rayleigh-wave microseisms, *Bull. Seism. Soc. Am.* **68**, 1623-1636.
- Báth, M. (1952). Review over investigations of microseisms in Scandinavia, *Pontif. Acad. Sci. Scripta Varia* **12**, 239-276.
- Boore, D. M. and M. N. Toksöz (1969). Rayleigh wave particle motion and crustal structure, *Bull. Seism. Soc. Am.* **59**, 331-346.
- Bungum, H., E. Rygg, and L. Bruland (1971). Short-period seismic noise structure at the Norwegian Seismic Array, *Bull. Seism. Soc. Am.* **61**, 357-373.
- Darbyshire, J. (1964). A study of microseisms in South Africa, *Geophys. J.* **8**, 165-175.
- D'Henry, G. (1950). Sulla natura fisica dei microsismi, *Ann. Geofis.* **2**, 281-289.
- Essen, H. H., H. B. Hirschleber, and J. Siebert (1973). Sound velocity and attenuation measurements on North Sea sediments, *Z. Geophys.* **39**, 833-854.
- Faust, L. Y. (1951). Seismic velocity as a function of depth and geologic time, *Geophysics* **16**, 192-206.
- Gutenberg, B. (1955). Untersuchungen zur Bodenunruhe in Südkalifornien, *Z. Geophys.* **21**, 177-190.
- Hasselmann, K. (1963). A statistical analysis of the generation of microseisms, *Rev. Geophys.* **1**, 177-210.
- Haubrich, R. A. and K. McCamy (1969). Microseisms; Coastal and pelagic sources, *Rev. Geophys.* **7**, 539-571.
- Heybroek, P., U. Haanstra and D. A. Erdman (1967). Observations on the geology of the North Sea area, *Proc. World Petroleum Congress, 7th, Mexico*; Elsevier, 905-916.
- Hinz, K. (1964). Zur Geologie der südlichen Nordsee nach reflexionsseismischen Untersuchungen, Diss. Bergakademie Clausthal, 87 pp.
- Hirschleber, H. B. (1975). Synthese der seismischen Krustenuntersuchungen in Jütland und den angrenzenden Gebieten, *Hamburger Geophysikal. Einzelschriften*, **29**, 110 pp.
- Jackson, D. D. (1972). Interpretation of inaccurate, insufficient and inconsistent data, *Geophys. J.* **28**, 97-109.
- Jenkins, G. M. and D. G. Watts (1968). *Spectral Analysis and Its Applications*, Holden Day, San Francisco, 541 pp.
- Lacoss, R. T., E. J. Kelly, and M. N. Toksöz (1969). Estimation of seismic noise structure using arrays, *Geophysics* **34**, 21-38.
- Nafe, J. E. and C. L. Drake (1957). Variation with depth in shallow and deep water marine sediments of porosity, density and the velocities of compressional and shear waves, *Geophysics* **22**, 523-552.
- Press, F. (1966). Seismic velocities, in *Handbook of Physical Constants*, S. P. Clark, Jr. Editor, *Geol. Soc. Am., Memoir* **97**.
- Schmalfeldt, B. (1978). Ein Vergleich von Mikroseismik- und Seegangsspektren und ein Versuch, die Anfachungsgebiete zu lokalisieren, *Hamburger Geophysikal. Einzelschriften* **35**, 53 pp.
- Searle, S. R. (1971). *Linear Models*, John Wiley, New York, 532 pp.
- Toksöz, M. N. and R. T. Lacoss (1968). Microseisms: Mode structure and sources, *Science* **159**, 872-873.
- Wiggins, R. (1972). The general linear inverse problem: implications of surface waves and free oscillations on earth structure, *Rev. Geophys. Space Phys.* **10**, 251-285.

INSTITUT FÜR GEOPHYSIK  
UNIVERSITÄT HAMBURG  
BUNDESSTRAßE 55  
D-2000 HAMBURG 13  
FEDERAL REPUBLIC OF GERMANY

Manuscript received July 16, 1979